Strong-coupling analysis of scanning tunneling spectra in Bi$_2$Sr$_2$Ca$_2$Cu$_3$O$_{10+\delta}$

C. Berthod, Y. Fasano,[*] I. Maggio-Aprile, A. Piriou, E. Giannini, G. Levy de Castro,[†] and Ø. Fischer

DPMC-MaNEP, Université de Genève, 24 quai Ernest-Ansermet, 1211 Genève 4, Switzerland

We study a series of spectra measured in the superconducting state of optimally doped Bi$_2$Sr$_2$Ca$_2$Cu$_3$O$_{10+\delta}$ (Bi-2223) by scanning tunneling spectroscopy. Each spectrum, as well as the average of spectra presenting the same gap, is fitted using a strong-coupling model taking into account the band structure, the BCS gap, and the interaction of electrons with the spin resonance. After describing our measurements and the main characteristics of the strong-coupling model, we report the whole set of parameters determined from the fits, and we discuss trends as a function of the gap magnitude. We also simulate angle-resolved photoemission spectra, and compare with recent experimental results.

I. INTRODUCTION

The two main single-electron spectroscopies, angle-resolved photoemission[1] (ARPES) and scanning tunneling microscopy[2] (STM), have considerably improved during the last decades, mainly motivated by the quest for reliable data in the study of cuprate high-temperature superconductors. A growing body of high-quality spectroscopic data is now available for the cuprates, especially for compounds of the bismuth family, which offer clean surfaces. These refined experiments on high-quality crystals may be able to deliver the intrinsic line shape of the one-electron spectra. Nonetheless, very few studies have undertaken a detailed line-shape study of the various spectral features by means of a microscopic model. Following pioneering studies,[3,4] the STM data analysis has remained mostly qualitative, or based on phenomenological approaches. In a few cases, a BCS d-wave model including a realistic band structure[5] and/or a phenomenological scattering rate[6] turned out to be appropriate. Such cases are the exception rather than the rule: These models will not capture, in particular, the "dip" feature ubiquitously present at energies above the superconducting gap. By analogy with phonon-related effects in classical superconductors,[7,8] the dip, also recently observed in pnictide superconductors,[9,10] is generally attributed to a collective mode. In order to analyze the phenomenon, an extension of the Eliashberg formalism to d-wave superconductors has been proposed.[11] Different interpretations, based on phonons,[12,13] an energy-dependent gap function,[14] gap inhomogeneities,[15] or a charge-density wave order,[16] have also been put forward.

In the superconducting state, the cuprates present a low-energy magnetic excitation known as the spin resonance. This excitation is observed below the superconducting critical temperature, T_c, by inelastic neutron scattering, as a strong enhancement of the spin susceptibility around the antiferromagnetic vector $\boldsymbol{Q} = (\pi/a, \pi/a)$. First discovered in YBa$_2$Cu$_3$O$_{6+x}$ (Y-123)[17,18] at an energy $\Omega_s = 41$ meV, it was later observed in most cuprates, including the single-layer compounds HgBa$_2$CuO$_{4+\delta}$[19] and Tl$_2$Ba$_2$CuO$_{6+\delta}$,[20] the two-layer Bi$_2$Sr$_2$CaCu$_2$O$_{8+\delta}$ (Bi-2212),[21–23] and the electron-doped material Pr$_{0.88}$LaCe$_{0.12}$CuO$_{4-\delta}$.[24] The (π,π) resonance energy ranges from 10 to 60 meV, roughly correlated with T_c as $\Omega_s \approx 5.3 k_B T_c$.[25] It is found in both underdoped and overdoped materials,[26] and was also observed above T_c in Y-123.[27] The

resonance has been interpreted as a spin-1 exciton, bound below the continuum of electron-hole excitations, gapped by the superconducting pairing.[28] One of the open questions concerns the role played by spin fluctuations, and particularly by the (π,π) resonance, in the pairing phenomenon.[29,30]

Being related to pair formation or not, the (π,π) resonance is a collective spin excitation, which must somehow interact with the charge degrees of freedom and induce renormalization and damping of the Bogoliubov quasiparticles in the superconducting state. This interaction affects the one-electron spectra and is observable in the single-electron spectroscopies. Although the strength of this interaction has been a matter of controversy,[31,32] there is evidence that peculiar signatures observed in photoemission,[33–36] tunneling,[37–41] and optical conductivity[42,43] result from this interaction. Yet, a firm consensus has not been reached: Optical phonons often exist in the cuprates at similar energies, and distinguishing the effects of the two kinds of excitations has proven difficult. The spin resonance, being localized near (π,π), leads to an anisotropic scattering rate and a strong dip.[39] But similar effects can be induced by phonons, provided that the electron-phonon coupling is strongly anisotropic.[12] A possible way of determining the origin of the dip feature is to study its evolution with doping, to be compared with the doping dependence of the spin resonance and phonons, both directly measured by neutron scattering.

In a d-wave superconductor, one of the signatures of the coupling to a collective mode is a *minimum*, so-called dip, in the electron density of states (DOS), occurring at an energy E_d, which is separated from the energy Δ_p (of the coherence peak) by the mode energy.[44] In contrast, for s-wave superconductors, the signature is a *change of curvature* of the DOS, leading to a peak in the DOS derivative.[45,46] Scanning tunneling microscopy/spectroscopy (STM/STS) allows one to measure the gap in the excitation spectrum, as well as the dip, with sub-meV and atomic resolutions, and to track their spatial variations in inhomogeneous materials.[40] It is therefore an ideal tool to investigate the properties of the dip and the relationship between the gap and the resonance energy. The three-layer compound Bi$_2$Sr$_2$Ca$_2$Cu$_3$O$_{10+\delta}$ (Bi-2223) is well suited for such studies. It can be cleaved and offers atomically flat surfaces for STM investigations. Bi-2223 has the highest optimal T_c of the bismuth family, 111 K, a gap in the

30–60 meV range, and a very strong dip as revealed by tunneling[47] and photoemission.[48–50]

In this paper, we study Bi-2223 STS spectra by means of least-squares fits to a strong-coupling model consisting of the Van Hove singularity (VHS) associated with the saddle point of a two-dimensional tight-binding band, a *d*-wave BCS gap, and a coupling to the (π,π) resonance.[44] The results of similar studies were reported previously.[39,40] Here, we describe our fits in detail, we fit average as well as local spectra, we provide and discuss the complete set of model parameters, and we use these parameters to simulate ARPES data. The motivation for performing direct *fits* to cuprate STS data is twofold. The first aim is to demonstrate that in spite of its simplicity, the model captures quantitatively the main characteristics of the data for optimally doped Bi-2223: a V-shaped gap at low energy, tall coherence peaks and very pronounced dips, both significantly electron-hole asymmetric. Second, the quality of these fits provides further evidence that the STS tunneling conductance measures the full *electron* local DOS (LDOS),[5] rather than an effective quasiparticle DOS deprived of band-structure and self-energy effects.[51]

In Sec. II, we describe the growth and characterization of the samples, present the measurement method, and discuss the main features of the spectra. Section III is dedicated to the model. We use different conventions than Ref. 44 for the model parameters. For definiteness, we describe and discuss our model in detail. We also explain the fitting method. In Sec. IV, we present our results and the trends in fitted parameters. We discuss the values of the most important parameters in Sec. V, compare with values obtained using other experimental techniques, and present simulations of ARPES intensities. Finally, Sec. VI is a summary of the results and implications of the present study.

II. EXPERIMENTAL DETAILS

A. Sample growth and characterization, STM measurements

The Bi-2223 crystals were grown by the traveling-solvent floating-zone method, as described in Ref. 52. In order to achieve optimal doping (OPT), the crystals were annealed during 10 days at 500 °C in 20 bar oxygen partial pressure. This thermal treatment produced a sharpening of the super-conducting transition with respect to the as-grown condition. We considered the peak position in the temperature derivative of the low-field susceptibility and in magnetization data as the criteria to determine T_c. Both determinations yielded the same $T_c = (110.5 \pm 0.5)$ K.[53] The transition width, estimated as the FWHM of the susceptibility and magnetization peaks, typically ranges between 0.6 and 2 K from sample to sample. The structural and superconducting properties of OPT crystals of the same batch as the ones studied here are reported in Refs. 53–56. X-ray diffraction measurements have revealed the purity and the high crystalline order of the samples.[55] Resistivity measurements showed a single and sharp su-perconducting transition. The sample growth and thermal treatment parameters were optimized, in order to suppress the intergrowth of the Bi-2212 phase. For the OPT samples studied here, Bi-2212 intergrowth, if present, represents less than 1% of the sample volume.[53]
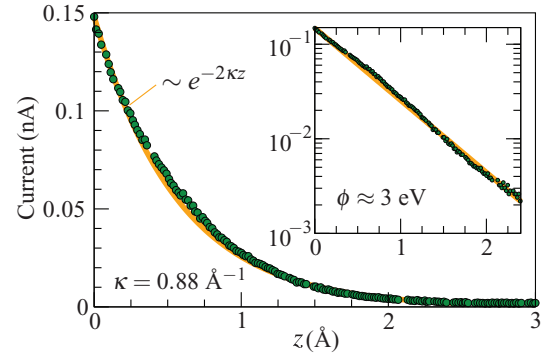
FIG. 1. (Color online) Decrease of the tunnel current with increasing tip-sample distance z for one of our junctions (circles). The solid line is an exponential fit. Inset: Same data on a log scale.

For the measurements, we used a home-built STM with ultrahigh-vacuum environment and ^{3}He base temperature.[57] Electrochemically etched iridium tips served as the ground electrode. The bias voltage V was applied to the sample, such that negative (positive) bias refers to occupied (empty) sample states. Differential-conductance spectra were acquired using a lock-in.[2] The dI/dV measurements were performed at fixed tip-sample distance, determined by regulation current and voltage of 0.6 nA and 600 mV, and a lock-in excitation amplitude of 2 mV. The samples were cleaved at room temperature at 1–5×10^{-9} mbar pressure, and cooled down to 2 K in 10 hours time. High-quality tunnel junctions were obtained in this way, as illustrated in Fig. 1. In a high-quality junction, the current depends exponentially on the relative tip-sample distance, namely $I \propto e^{-2\kappa z}$. The decay constant κ is related to the apparent barrier height $\phi = \hbar^2 \kappa^2/(2m)$. Our tunnel junctions have typically $\phi = 3$–4 eV, much larger than the regulation voltage. We started all our runs of measurements with tests like the one shown in Fig. 1.

B. Data statistics and systematics of spectral features

As largely documented in the literature, Bi-based cuprate samples, even with a sharp superconducting transition, present inhomogeneous spectroscopic properties on the surface.[2] The nanoscale variations of typical spectral features in Bi-2223 were studied previously by mapping the local dI/dV curves.[40] It was found, in particular, that the local gap Δ_p presents spatial variations in register with the crystalline structure. The present paper is focused on studying relevant spectral features as a function of Δ_p. Since the results in several OPT samples are similar, for the present study we considered 150 spectra measured at different locations of a given OPT sample. The local dI/dV curves were sorted by half the peak-to-peak gap $\Delta_p = (\Delta_p^+ - \Delta_p^-)/2$, where Δ_p^+ (Δ_p^-) is the energy of the coherence peak at positive (negative) bias. Figure 2 shows the set of spectra, as well as the average spectra for each Δ_p (the latter were already published in Ref. 39). The standard deviation to the average is also shown as a function of bias. It is generally $\sim$5%, except close to the coherence peaks where it increases up to 20%. This is a hallmark of the lock-in technique, which is most reliable for slowly varying $I(V)$ curves.
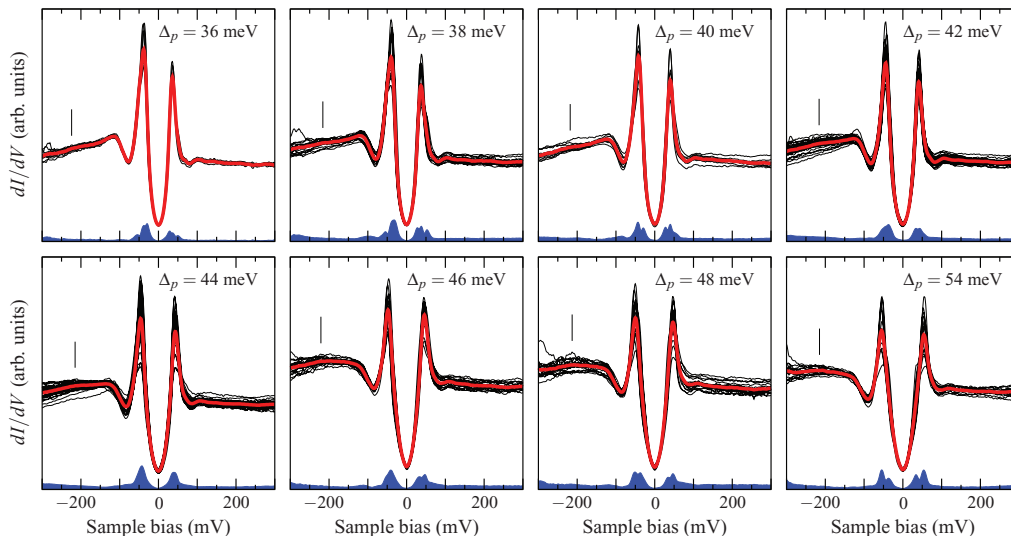
FIG. 2. (Color online) The complete experimental data set considered in this study. The raw Bi-2223 tunneling conductance spectra were grouped according to their peak-to-peak gap Δ_p, and were normalized in order to have the same spectral weight in the range of the figure (black curves). The red curves are the average spectra, and the shaded blue curves show the standard deviation of the distribution of tunneling conductances at each bias. The vertical bars indicate a weak feature, possibly related to the VHS of the inner-layer band (see Sec. III).

The prominent spectral features of Bi-2223 are evident from the average dI/dV curves in Fig. 2. All spectra present a d-wave shape at low bias, very well developed coherence peaks, and a dip at energies larger than Δ_p. Another remarkable property is a strong electron-hole asymmetry, characterized by a stronger dip and a greater spectral weight for the occupied states. This is manifested by higher coherence peaks and an enhanced conductance background at negative bias. Observed in most high T_c's, this phenomenology contrasts with the electron-hole symmetric spectra of classical superconductors.

The electron-hole asymmetry evolves monotonically with Δ_p. The conductance background for occupied states becomes steeper on decreasing the gap. The trend is particularly evident when considering data in a bias range one order of magnitude larger than Δ_p. This evolution may be due to a variation of the correlation effects with the pairing strength.[51] Since our model does not consider such correlations, we will restrict our fits to the bias interval [−150, + 150] mV. Moreover, the asymmetry in the height of the coherence peaks systematically increases when decreasing Δ_p. We discuss the role of the VHS in this phenomenology in Secs. III C and V. The line shape of the coherence peaks also follows a monotonic trend. The peaks sharpen and become taller on approaching the Fermi energy. The evolution of the dip is of particular importance for this work. This feature is strongly developed in Bi-2223, in comparison to other Bi-based cuprates, and is noticeably electron-hole asymmetric. The energy difference between the dip minimum and the coherence peak maximum decreases on increasing the gap,[40] as we will discuss in the following sections.

Finally, the low-energy conductance is similar for all values of Δ_p. Close to the Fermi level, the spectra are electron-hole symmetric and present a slightly rounded shape. A V-shaped conductance is characteristic of a d-wave superconductor at zero temperature. Some rounding off and a finite zero-bias conductance are expected when considering thermal and mea-surement broadening—the latter due to the finite amplitude of the lock-in excitation and to electronic noise—and some residual impurity scattering. Our fitting procedure takes these factors into account.

III. STRONG-COUPLING MODEL AND FITTING PROCEDURE

A. STM tunneling conductance and LDOS

The theory of tunneling in superconductors was origi-nally meant for planar junctions involving classical s-wave superconductors, with a structureless normal-state DOS.[45] The theory of Tersoff and Hamann for the STM,[58] on the other hand, was not developed for superconductors. The approach of Ref. 58 can be extended to describe STM measurements in superconductors,[2] and leads to the paradigm that the differential conductance is a measure of the thermally broadened electron LDOS:

$$\frac{dI(\boldsymbol{r})}{dV} = M \int_{-\infty}^{\infty} d\omega d\varepsilon \, N(\boldsymbol{r},\omega)[-f'(\omega - \varepsilon)] g_{\sigma}(\varepsilon - eV).$$

$$(1)$$

This expression applies if the current is dominated by single-particle tunneling. $N(\boldsymbol{r},\omega)$ is the sample LDOS at the position $\boldsymbol{r}$ of the STM tip, f' is the derivative of the Fermi function, and M is a tip-dependent constant. An extra Gaussian broadening by the function g_{σ} takes into account the finite experimental resolution, with σ the half width at half maximum. In addition to electronic noise, the sources of broadening are the lock-in ac modulation and the averaging of several similar spectra (see Sec. II). The strict proportionality of dI/dV and $N(\boldsymbol{r},eV)$ is recovered in the limits of zero temperature and $\sigma = 0$, where both $-f'$ and g_{σ} become delta functions.

If the work function is much larger than the typical energies of interest (in our case, 3 eV compared with 0.1–0.2 eV;

see Fig. 1), all Bloch waves decay exponentially outside the sample surface with a similar decay constant κ. The LDOS at $\boldsymbol{r}$ reduces to $N(\boldsymbol{r},\omega) \propto \exp(-2\kappa z)N(\omega)$, with $N(\omega)$ the bulk two-dimensional DOS, assumed translation invariant in the (x,y) plane for simplicity. Consistently, the current must decrease exponentially with z, as confirmed in Fig. 1. The z dependence is irrelevant in spectroscopic measurements, and $N(\boldsymbol{r},\omega)$ in Eq. (1) can be replaced by $N(\omega)$, with a redefinition of the constant M. We then calculate the two-dimensional DOS as the integral of the electron spectral function:

$$N(\omega) = \frac{2}{N} \sum_{\boldsymbol{k}} (-1/\pi) \operatorname{Im} G_{11}(\boldsymbol{k},\omega). \tag{2}$$

G_{11} is the first component of the Green's function in the Nambu representation, and N is the number of $\boldsymbol{k}$ points in the two-dimensional Brillouin zone. In a superconductor characterized by a BCS gap $\Delta_{\boldsymbol{k}}$ and inelastic scattering processes, it is convenient to write G_{11} in terms of the 2×2 matrix self-energy $\hat{\Sigma}(\boldsymbol{k},\omega)$, in the form

$$G_{11} = \left[\omega - \xi_{\boldsymbol{k}} + i\Gamma - \Sigma_{11} - \frac{(\Delta_{\boldsymbol{k}} + \Sigma_{12})^2}{\omega + \xi_{\boldsymbol{k}} + i\Gamma - \Sigma_{22}} \right]^{-1}. \tag{3}$$

$\Sigma_{11}(\boldsymbol{k},\omega)$ and $\Sigma_{22}(\boldsymbol{k},\omega)$ describe the renormalization and damping of the Bogoliubov quasiparticles in the electron and hole branches, respectively, while the "anomalous" self-energy $\Sigma_{12}(\boldsymbol{k},\omega)$ describes scattering effects in the pairing channel. The expression of $\hat{\Sigma}$ is provided in the next subsection. If $\hat{\Sigma} = 0$, Eq. (3) reduces to the BCS Green's function, with $\xi_{\boldsymbol{k}} \equiv \varepsilon_{\boldsymbol{k}} - \mu$ the noninteracting electron dispersion, μ the chemical potential, and Γ a phenomenological scattering rate.[59] We use a tight-binding model for the band $\varepsilon_{\boldsymbol{k}}$, which reads (setting the lattice parameter $a \equiv 1$)

$$\begin{aligned} \varepsilon_{\boldsymbol{k}} &\equiv \sum_{\boldsymbol{r}} t(|\boldsymbol{r}|) \, e^{i\boldsymbol{k}\cdot\boldsymbol{r}} \\ &= 2t_1(\cos k_x + \cos k_y) + 4t_2 \cos k_x \cos k_y \\ &\quad + 2t_3(\cos 2k_x + \cos 2k_y) + 4t_4(\cos 2k_x \cos k_y \\ &\quad + \cos k_x \cos 2k_y) + 4t_5 \cos 2k_x \cos 2k_y. \end{aligned} \tag{4}$$

Note that our conventions for the signs and magnitudes of the hopping amplitudes t_i differ from those used in Ref. 44. The d-wave gap is $\Delta_{\boldsymbol{k}} = \Delta_0(\cos k_x - \cos k_y)/2$.

Bi-2223 has three CuO$_2$ layers per unit cell, hence three bands at the Fermi level.[60] Recent photoemission studies suggest that the bands form a nearly degenerate doublet, attributed to the outer CuO$_2$ layers, and a single band associated with the inner CuO$_2$ layer.[61,62] The inner-layer band is seen $\sim$70 meV ($\sim$200 meV) below the doublet in the nodal (antinodal) direction. We found that a one-band model focusing on the doublet, with fewer adjustable parameters than a three-band model, is sufficient to fit the spectra in the range $|\omega| < 150$ meV. This can be understood, since the doublet carries 2/3 of the spectral weight, and the VHS of the inner-layer band lies $\sim$200 meV below that of the doublet, at the border of our measurement window. We expect that the modifications induced in the theoretical spectrum by using a multiband description would be marginal at low energies. That

said, we note that the average spectra in Fig. 2 systematically present a weak structure at negative bias, between -215 and -225 mV, which might be the signature of the inner-layer VHS. Although a definitive assessment is not possible at this stage, this observation confirms that possible multiband effects are likely to be small.

B. Bogoliubov quasiparticles coupled to spin fluctuations

The theoretical investigation of the coupling between Bogoliubov quasiparticles and spin fluctuations began with the study of the superfluid transition in ^{3}He (see Ref. 63 and references therein), and was revived after the discovery of high-T_c superconductors.[64–66] The minimal model to describe the effects of this coupling is

$$\begin{aligned} \hat{\Sigma}(\boldsymbol{k},\omega) = &-\frac{1}{N} \sum_{\boldsymbol{q}} \frac{1}{\beta} \sum_{i\Omega_n} g^2 \chi_s(\boldsymbol{q},i\Omega_n) \\ &\times \left. \hat{\mathscr{G}}_0(\boldsymbol{k}-\boldsymbol{q},i\omega_n - i\Omega_n) \right|_{i\omega_n \to \omega + i0^+}. \end{aligned} \tag{5}$$

$\hat{\mathscr{G}}_0$ is the 2×2 Nambu-BCS-Matsubara Green's function in the absence of coupling, χ_s is the spin susceptibility, $i\omega_n$ and $i\Omega_n$ are the fermionic and bosonic Matsubara frequencies, respectively, $\beta = (k_{\mathrm{B}}T)^{-1}$ is the inverse temperature, and g is the coupling parameter. Equation (5) can be obtained from perturbation theory in the electron-spin coupling;[67] it can also be viewed as a simplified, non-self-consistent version of a conserving strong-coupling theory.[68]

Following Ref. 44, we use a separable phenomenological expression for χ_s in the superconducting state. In the energy range of interest (below ~ 150 meV), we assume that the spin response is dominated by a resonance at energy Ω_s, near the antiferromagnetic vector $\boldsymbol{Q} = (\pi,\pi)$:

$$\chi_s(\boldsymbol{q},i\Omega_n) = W_s \, F(\boldsymbol{q}) \int_{-\infty}^{\infty} d\varepsilon \, \frac{I(\varepsilon)}{i\Omega_n - \varepsilon}. \tag{6}$$

We choose the real functions $F(\boldsymbol{q})$ and $I(\varepsilon)$ such that $(1/N) \sum_{\boldsymbol{q}} F(\boldsymbol{q}) = \int_0^{\infty} d\varepsilon \, I(\varepsilon) = 1$. W_s thus stands for the momentum and frequency integrated spectral weight of the resonance:

$$W_s = \frac{1}{N} \sum_{\boldsymbol{q}} \int_0^{\infty} d\omega \, (-1/\pi) \operatorname{Im} \chi_s(\boldsymbol{q},\omega). \tag{7}$$

The function $F(\boldsymbol{q})$ is Lorentzian-like, peaked at $\boldsymbol{q} = \boldsymbol{Q}$, with half width at half maximum Δq:

$$F(\boldsymbol{q}) = \frac{F_0}{\sin^2\left(\frac{q_x - Q_x}{2}\right) + \sin^2\left(\frac{q_y - Q_y}{2}\right) + (\Delta q/4)^2}. \tag{8}$$

The constant F_0 ensures the normalization of $F(\boldsymbol{q})$. In Ref. 44, the resonance was assumed to be sharp in energy, so that its energy distribution was $I(\varepsilon) = \delta(\varepsilon - \Omega_s) - \delta(\varepsilon + \Omega_s)$. Indeed, neutron scattering measurements suggest that the resonance is resolution limited in Y-123.[17] We use a slightly more general form,

$$I(\varepsilon) = I_0 \left[L_{\Gamma_s}(\varepsilon - \Omega_s) - L_{\Gamma_s}(\varepsilon + \Omega_s) \right], \tag{9}$$

where $L_{\Gamma}(\varepsilon) = (\Gamma/\pi)/(\varepsilon^2 + \Gamma^2)$ is a Lorentzian, and I_0 ensures the normalization of $I(\varepsilon)$. The form (9) accounts for a

finite lifetime $\tau_s \sim \Gamma_s^{-1}$ of the spin mode. Neutron scattering experiments indicate that the resonance is somewhat broader in Bi-2212 (Ref. [21]) and Bi-2223 (Ref. [69]) than in Y-123, and would be consistent with $\Gamma_s \approx 4$–8 meV. Alternatively, Eq. (9) may be regarded as a way to incorporate the observed dispersion of the resonance,[70] which broadens the mode into a band of width Γ_s.

It is convenient to write the Matsubara Green's function in Eq. (5) using the spectral representation,

$$\hat{\mathcal{G}}_0(\boldsymbol{k}, i\omega_n) = \int_{-\infty}^{\infty} d\varepsilon \, \frac{\hat{A}(\boldsymbol{k}, \varepsilon)}{i\omega_n - \varepsilon}. \qquad (10)$$

Taking into account the phenomenological scattering rate Γ appearing in Eq. (3), the spectral function can be expressed in terms of Lorentzian functions,

$$\hat{A}(\boldsymbol{k}, \varepsilon) = \hat{u}_{\boldsymbol{k}} L_{\Gamma}(\varepsilon - E_{\boldsymbol{k}}) + \hat{v}_{\boldsymbol{k}} L_{\Gamma}(\varepsilon + E_{\boldsymbol{k}}), \qquad (11)$$

where

$$\hat{u}_{\boldsymbol{k}} = \frac{1}{2} \begin{pmatrix} 1 + \frac{\xi_{\boldsymbol{k}}}{E_{\boldsymbol{k}}} & \frac{\Delta_{\boldsymbol{k}}}{E_{\boldsymbol{k}}} \\ \frac{\Delta_{\boldsymbol{k}}}{E_{\boldsymbol{k}}} & 1 - \frac{\xi_{\boldsymbol{k}}}{E_{\boldsymbol{k}}} \end{pmatrix}, \quad \hat{v}_{\boldsymbol{k}} = \mathbb{1} - \hat{u}_{\boldsymbol{k}}, \qquad (12)$$

and $E_{\boldsymbol{k}} = \sqrt{\xi_{\boldsymbol{k}}^2 + \Delta_{\boldsymbol{k}}^2}$. After inserting Eqs. (6) and (10) in Eq. (5), one performs the sum over Matsubara frequencies with the standard technique,[71] and using Eqs. (9) and (11), one obtains the self-energy on the real-frequency axis:

$$\hat{\Sigma}(\boldsymbol{k}, \omega) = \frac{\alpha^2}{N} \sum_{\boldsymbol{q}} F(\boldsymbol{q}) [\hat{u}_{\boldsymbol{k}-\boldsymbol{q}} B(\omega, E_{\boldsymbol{k}-\boldsymbol{q}})$$
$$+ \hat{v}_{\boldsymbol{k}-\boldsymbol{q}} B(\omega, -E_{\boldsymbol{k}-\boldsymbol{q}})]. \qquad (13)$$

We have introduced the dimensionless coupling constant $\alpha^2 \equiv (g/\Lambda)^2 W_s I_0$, with Λ a characteristic energy scale of the model, which we take as the nearest-neighbor hopping t_1. For definiteness, the function $B(\omega, E)$ is derived in the Appendix. The self-energy (13) is a convolution in momentum space, and can therefore be efficiently evaluated numerically on dense $\boldsymbol{k}$-point meshes, using fast Fourier transforms.

The use of a coupling constant α comprising the spectral weight of the resonance, instead of the coupling g, is more convenient for our purposes. The strength of the self-energy effects—hence the strength of the dip in the tunneling spectrum—is governed by the product $g^2 W_s$, and W_s strongly depends on the momentum width Δq of the resonance. In the original formulation,[44] both g and Δq strongly affect the dip, whereas here, the dip is controlled mostly by α, and depends weakly on Δq. As the model parameters will be determined by least-squares fits, we expect a simpler landscape by avoiding that different parameters have the same influence on the theoretical spectrum.

C. Discussion of the model

The model has fifteen parameters, including the multiplicative constant M in Eq. (1), thirteen of which are determined by least-squares fitting. The two fixed parameters are the temperature (set to the experimental value $T = 2$ K) and the Gaussian broadening σ (set to 4 meV). We constrain the scattering rate Γ to be larger than 1 meV for the numerical stability of the momentum sum in Eq. (2). The scale of the
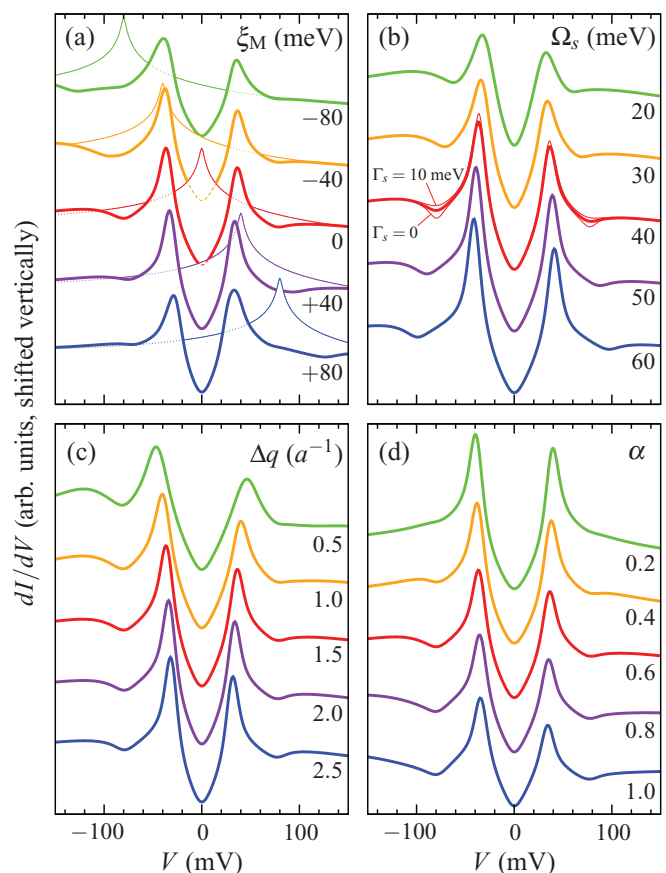
FIG. 3. (Color online) Evolution of the theoretical tunneling spectrum with varying five model parameters. The base parameters are (all energies in meV) $M = 1$, $\Gamma = 2$, $t_{1-5} = (-250, 80, 0, 0, 0)$, $\mu = -320$, $\Delta_0 = 40$, $\Omega_s = 40$, $\Gamma_s = 5$, $\Delta_q = 1.5/a$, $\alpha = 0.6$, and they correspond to the middle red curve in each series. The $\boldsymbol{k}$-point mesh contains 1024×1024 points. In (a), the chemical potential is varied to move the Van Hove singularity from -80 to $+80$ meV; the thin lines show the corresponding noninteracting DOS (i.e., with $\Delta_0 = 0$ and $\alpha = 0$). (b), (c), and (d) show the result of varying the resonance energy Ω_s, $\boldsymbol{q}$-space width Δq, and the coupling α, respectively. The effect of changing Γ_s is illustrated by the thin curves in (b).

d-wave gap is set by Δ_0 and modified by the coupling to the spin resonance, as discussed further below.

The band parameters t_{1-5} and the chemical potential μ determine the noninteracting DOS, the band filling, and the Fermi surface. The tunneling spectrum is very sensitive to the energy of the VHS given by the dispersion at the M point $(\pi, 0)$, $\xi_M = 4(-t_2 + t_3 + t_5) - \mu$, as illustrated in Fig. 3(a). Four trends can be observed: The energy of the VHS affects (1) the difference in height of the two coherence peaks, (2) the electron-hole asymmetry of the dip, (3) the overall height of the coherence peaks, and (4) the half peak-to-peak gap Δ_p. (1) is due to the superconducting gap, pushing the VHS farther down if initially at negative energy, and farther up in the opposite case. The coherence peak closest to the VHS thus carries more spectral weight. One notices that some electron-hole asymmetry remains when $\xi_M = 0$, because a finite t_2 breaks the electron-hole symmetry of the noninteracting DOS. (2) is a consequence of the dip being reinforced by the VHS

and therefore strongest at negative energy if $\xi_M < 0$, and vice versa.[39] (3) reveals the contribution of the VHS to the weight of the coherence peaks, tallest when $\xi_M = 0$. Lastly, (4) is a consequence of d-wave symmetry, implying that the maximum gap on the Fermi surface decreases as the distance between the Fermi crossing in the antinodal direction and the M point increases.

Varying the resonance energy Ω_s has three main effects, as shown in Fig. 3(b): (1) The dip minimum moves with respect to the closest coherence peak, (2) the height of the coherence peaks changes, and (3) the gap Δ_p varies. (1) indicates that the scattering is strongest near the energy $\Delta_0 + \Omega_s$: Bogoliubov quasiparticles at this energy can easily decay by emitting a (π, π) mode, because there are many final states available near the gap-edge energy Δ_0. One can figure out the typical energy dependence of the scattering rate by using the limit (A8) for the function B, and averaging Eq. (13) over the Brillouin zone. One arrives at

$$-\text{Im}\,\bar{\Sigma}_{11}(\omega) = \frac{\pi}{2}(\alpha t_1)^2[\theta(\omega - \Omega_s)N_0(\omega - \Omega_s) \\ + \theta(-\omega - \Omega_s)N_0(\omega + \Omega_s)], \qquad (14)$$

where $N_0(\omega)$ is the d-wave BCS DOS. Since $N_0(\omega)$ peaks at $\omega \approx \pm\Delta_0$, $-\text{Im}\,\bar{\Sigma}_{11}(\omega)$ peaks at $\omega \approx \pm(\Delta_0 + \Omega_s)$. Due to the confinement of the resonance around (π, π), the amplitude of the scattering rate has a marked momentum dependence.[44,46] Still, Eq. (14) correctly captures the qualitative energy dependence at all momenta. The effect (2)—increase of the peaks' height with increasing Ω_s—can also be understood based on Eq. (14): The scattering rate is zero for $|\omega| < \Omega_s$, since Bogoliubov quasiparticles cannot decay, and thus the coherence peaks are not broadened if $\Omega_s > \Delta_p$. The broadening is strongest when the peak in $-\text{Im}\,\bar{\Sigma}_{11}$ coincides with Δ_p, i.e., when $\Omega_s \to 0$. The origin of trend (3) is in the renormalization of the quasiparticle energies, encoded in the real part of the self-energy. The latter is linear at low energy, $\text{Re}\,\bar{\Sigma}_{11}(\omega) \approx -\bar{\lambda}\omega$, and the energy levels are renormalized by a factor $1/(1 + \bar{\lambda})$. Performing the Brillouin-zone average as above leads to

$$\bar{\lambda} = (\alpha t_1)^2 \frac{1}{2} \int_{-\infty}^{\infty} d\varepsilon\, \frac{N_0(\varepsilon)}{(|\varepsilon| + \Omega_s)^2}. \qquad (15)$$

If the Fermi point in the antinodal direction is close to the M point, the scale Δ_p is given to a good approximation by $\Delta_0(1 + \Psi_M)/(1 + \lambda_M)$. λ_M is the renormalization at the M point, which is typically 30% larger than the Brillouin-zone average $\bar{\lambda}$, and $\Psi_M = \text{Re}\,\Sigma_{12}(M, 0)/\Delta_0$ gives the contribution of the spin resonance to pairing. Ψ_M is a decreasing function of Ω_s. This can be seen by estimating the Brillouin-zone average of $\text{Re}\,\Sigma_{12}(\boldsymbol{k}, 0)/\Delta_{\boldsymbol{k}}$, which gives

$$\bar{\Psi} \approx (\alpha t_1)^2 \int_0^{\infty} d\varepsilon\, \frac{N_0(\varepsilon)}{\varepsilon(\varepsilon + \Omega_s)}. \qquad (16)$$

Equation (16) is accurate in the limit $\Delta q \to 0$ and for an electron-hole symmetric band. Looking at the Ω_s dependence of $\bar{\Psi}$, one expects a decrease of Δ_p with increasing Ω_s. However, this is overcompensated by the faster decrease of $\bar{\lambda}$ with Ω_s [see Eq. (15)], and the net result is a slight increase of Δ_p with increasing Ω_s, as seen in Fig. 3(b). This figure also

illustrates the effect of increasing Γ_s, namely, a broadening mostly confined to the neighborhood of the dip minimum.

Figure 3(c) shows that the momentum width of the resonance affects the gap renormalization. If $\Delta q \lesssim a^{-1}$, Ψ_M wins over λ_M, and $\Delta_p > \Delta_0$, while the opposite happens if $\Delta q \gtrsim a^{-1}$. The precise value of Δq where this change of behavior takes place depends on the other model parameters. For $\Delta q \to 0$, the renormalizations at M can be evaluated as

$$\lambda_M = \frac{(\alpha t_1)^2}{(E_M + \Omega_s)^2}, \quad \Psi_M = \frac{(\alpha t_1)^2}{E_M(E_M + \Omega_s)} \quad (\Delta q = 0),$$
$$(17)$$

and indeed $\Psi_M > \lambda_M$ in this case $(E_M = \sqrt{\xi_M^2 + \Delta_0^2})$. In the opposite limit, $\Delta q \to \infty$ or $F(\boldsymbol{q}) \equiv 1$, the self-energy becomes momentum independent. We then simply get

$$\lambda_M = \bar{\lambda}, \quad \Psi_M = 0 \quad (\Delta q = \infty), \qquad (18)$$

and the gap is reduced by a factor $1/(1 + \bar{\lambda})$. The vanishing of Ψ_M is due to the d-wave symmetry of $\Delta_{\boldsymbol{k}}$. We emphasize that the variation in Fig. 3(c) is performed at *fixed spectral weight* of the resonance, meaning that the bare coupling g decreases as Δq increases, and α remains unchanged. The value of Δq also influences the height of the coherence peaks: They are strongly broadened when the renormalized gap is larger than Ω_s, as in Fig. 3(b).

Finally, changing the dimensionless coupling α produces three effects, as seen in Fig. 3(d). Increasing α (1) digs the dip, (2) reduces the gap, and (3) lowers the coherence peaks without broadening them. The fact that the scattering rate is proportional to α^2 [Eq. (14)] explains (1). (2) is due to the fact that $\Delta q > a^{-1}$ ($\Psi_M < \lambda_M$) in Fig. 3(d), as discussed previously; since both Ψ_M and λ_M are $\propto \alpha^2$, $(1 + \Psi_M)/(1 + \lambda_M)$ decreases with increasing α. Finally, the effect (3) reflects the removal of low-energy spectral weight by the coupling to the resonance. This weight is transferred to the "hump," but also over larger energy scales, to the band edges. This is demonstrated in Fig. 4, showing the data of Fig. 3(d) on an expanded energy range. We further note that part of the spectral weight removed in the dip is also pushed to *lower* binding energies and, under certain conditions, can lead to shoulders on the sides of the coherence peaks.

We close this section with a few general remarks. Unlike in the conventional strong-coupling theory, the model used here
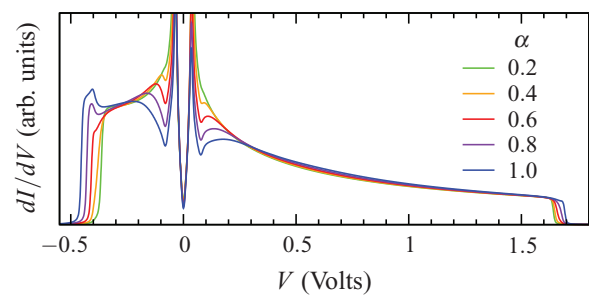
FIG. 4. (Color online) Same data as Fig. 3(d) on an expanded energy range covering the whole bandwidth. Part of the low-energy spectral weight is transferred to the band edges.

does not offer simple relationships between the parameters and prominent features in the tunneling spectrum. Each feature is controlled by several parameters. For instance, the gap Δ_p depends on Δ_0, ξ_M, Ω_s, Δq, and α, as illustrated in Fig. 3. A direct readout of the parameters by inspection of the spectra is possible qualitatively, but fitting is required for extracting accurate values. One peculiarity of the spectrum, however, can be attributed to a single cause: the electron-hole asymmetry—of the coherence peaks' height, dip strength, and conductance background—has only one source: the electron-hole asymmetry of the noninteracting DOS. Therefore, the qualitative inference of an asymmetric normal DOS *can* be made by direct inspection of the spectra. Finally, we emphasize that although the contribution of the anomalous self-energy to pairing is always positive, Δ_p may eventually turn out to be smaller than Δ_0, due to the normal self-energy renormalization. Namely, the coupling to the spin resonance contributes positively to pairing, but can nevertheless reduce the preexisting gap.

D. Fitting procedure and variance of the parameters

The 13-parameter landscape is too complex for a brute-force fitting approach. The reason is that the theoretical spectrum depends on properties of the noninteracting DOS, such as the position and asymmetry of the VHS, that are not in one-to-one correspondence with the set of hopping amplitudes t_i.[72] A least-squares fit starting with random values of the parameters will almost certainly end in a local minimum, where the t_i values do not satisfy physical requirements such as the order of magnitude of the bandwidth. The fit must therefore be guided with a pinch of physical intuition, in order to avoid such minima.

In a first step, we have considered the average spectra of Fig. 2. For each of them, we searched a set of parameters which (i) is a minimum of the least-squares function,[73] (ii) corresponds to a band with the properties shared by all Bi-based cuprates—band minimum at Γ, band maximum at (π,π), VHS at M—and (iii) gives a holelike Fermi surface centered at (π,π). The actual procedure was to search good parameters for the spectra with $\Delta_p = 36$ and 54 meV (this required a bit of trial and error), and then to use interpolations between these parameters as seeds to fit the average spectra with intermediate gaps. The fits were restricted to the energy window $|\omega| < 150$ meV.

In a second step, we calculated the distributions of the parameters associated with the sample inhomogeneity, and leading to the fluctuations of individual spectra around the average (see Fig. 2). We fitted all individual spectra, using as seeds the values obtained for the corresponding average spectrum, and leaving all parameters free to vary without constraint. Figure 5 shows all individual fits for one of the series in Fig. 2, and the distributions of fitted values for three important parameters. For all parameters, we find that the average of the distribution coincides with the value obtained by fitting the average spectrum, within the standard deviation (see Fig. 8 below). This justifies the use of average spectra to cope with the fluctuations seen in Figs. 2 and 5.
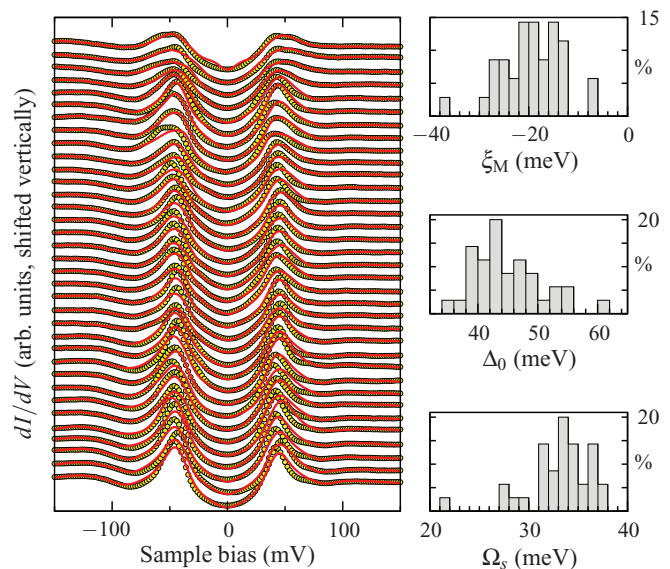
FIG. 5. (Color online) Series of experimental spectra with a peak-to-peak gap $\Delta_p = 44$ meV (yellow circles), and fits to the strong-coupling model (red lines). The histograms show the distributions of fitted values for the energy of the VHS, the BCS gap, and the spin-resonance energy. Similar results are obtained for all series in Fig. 2. The standard deviations of the distributions reflect the sample inhomogeneity, and are given for all parameters in Table I.

IV. RESULTS

Figure 6 presents the results of our fits to the average spectra, and Table I lists the set of fitted parameters, as well as the standard deviations. The model can reproduce the relative values of the conductance at zero bias, on the coherence peaks, and on the background, as they vary with increasing Δ_p. It also captures the electron-hole asymmetry of the coherence peaks, and the decrease of this asymmetry with increasing Δ_p. The electron-hole asymmetry of the dip can be followed as a function of Δ_p, even when the coherence peaks have become almost symmetric, at $\Delta_p = 54$ meV. Good fits can also be achieved in the full energy range of Fig. 2, at the price of a slight deterioration of the fit at low energies, especially for the largest gaps. The progressive inadequacy of the model for increasing energy range can have various causes. The presence in the experimental spectrum of components not considered in the model is one possibility, for instance, the contribution of the inner-layer band, or an enhanced spectral weight of the occupied states due to correlations.[47] Another possibility would be additional scattering mechanisms at high energy, in particular by the continuum of spin fluctuations.[44]

Before discussing the parameters, we emphasize three assertions which are supported by the quality of the fits in Fig. 6. First, STS measures the local *electron* DOS, including band-structure effects: It is not possible to subtract or divide out the noninteracting DOS by normalization. Second, the presence of the Van Hove singularity in the noninteracting DOS is crucial to reproduce the various asymmetries of the spectra: This is the *only* source of electron-hole asymmetry in the model. Third, a coupling to the spin resonance can explain quantitatively the redistribution of spectral weight around the dip energy. The tight localization of the resonance around
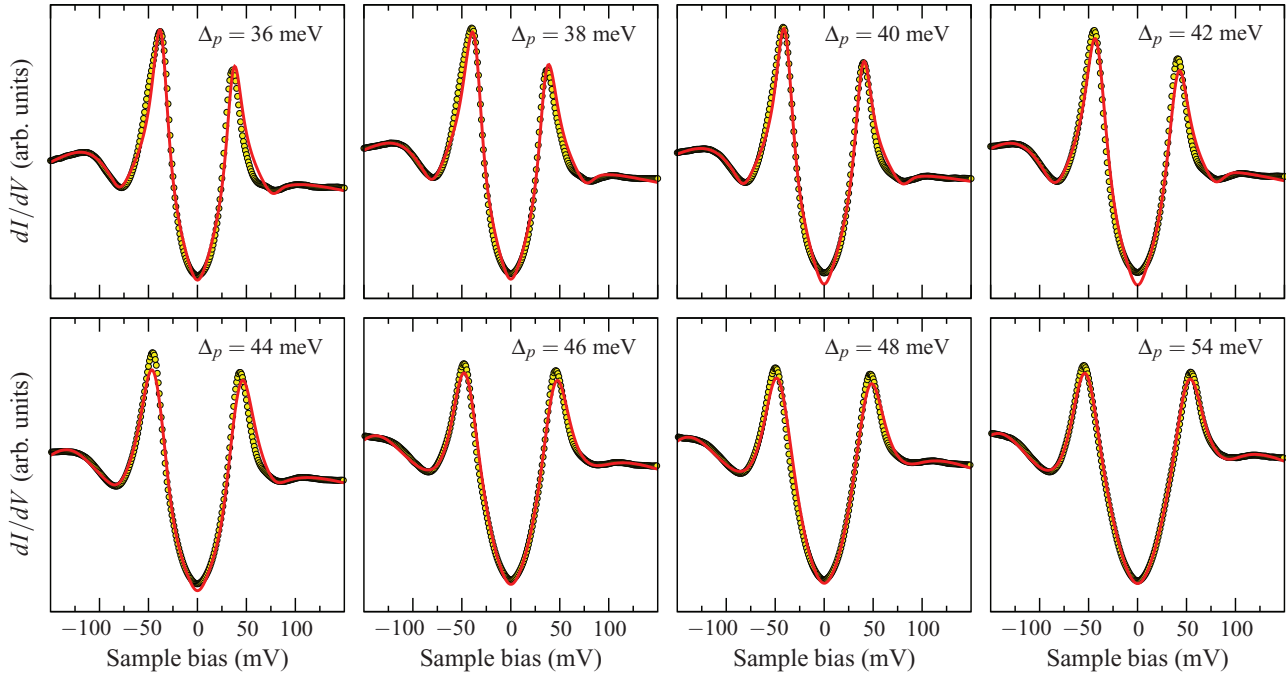
FIG. 6. (Color online) Average spectra of Fig. 2 (circles) and fits with the model described in Sec. III (red curves). The parameters are given in Table I.

(π,π), as opposed to optical phonons that span the whole Brillouin zone, plays a key role in producing the correct line shape of the dip.

Table I shows that large uncertainties are associated with the t_i's. This illustrates the weak sensitivity of the theoretical spectrum to the band parameters (see Sec. III D). The nearest-neighbor hopping t_1 varies between -140 and -256 meV:

These numbers fall within the range of published values for Bi-based cuprates.[44,74–76] The hopping t_3 (second neighbor along the Cu-Cu direction) is negative like t_1, as expected from symmetry considerations. Likewise, the diagonal hoppings t_2 and t_5 are both positive, or the latter is almost zero (we consider the small negative values of order 1 meV as insignificant). We do not try to interpret the variations of the t_i with increasing

TABLE I. Model parameters: For each experimental gap Δ_p and each parameter, the first column gives the value obtained by fitting the average spectrum (Fig. 6); the number in parentheses is the standard deviation of the values obtained by fitting all individual spectra, as illustrated in Fig. 5.

Δ_p (meV)	Parameters of the dispersion					
	μ (meV)	t_1 (meV)	t_2 (meV)	t_3 (meV)	t_4 (meV)	t_5 (meV)
36	-165 (56)	-180 (43)	32 (24)	-11 (10)	2.2 (8.6)	-1.6 (3.7)
38	-125 (111)	-161 (79)	21 (36)	-14 (17)	5.8 (9.3)	-1.4 (6.3)
40	-101 (105)	-140 (85)	3 (46)	-23 (21)	11.9 (15.5)	-3.4 (4.1)
42	-116 (51)	-162 (46)	18 (26)	-17 (13)	4.3 (9.2)	-0.8 (3.5)
44	-237 (108)	-206 (217)	56 (50)	-36 (93)	-10.3 (39.9)	27.9 (42.0)
46	-306 (73)	-179 (66)	59 (43)	-79 (49)	-22.6 (12.6)	56.6 (16.6)
48	-340 (108)	-206 (109)	60 (52)	-97 (55)	-26.3 (9.3)	67.0 (24.9)
54	-305 (146)	-256 (87)	58 (44)	-88 (73)	-35.4 (15.9)	62.9 (25.6)
	Scattering rate, BCS gap, and spin resonance					
	Γ (meV)	Δ_0 (meV)	Ω_s (meV)	Γ_s (meV)	Δq (a^{-1})	α
36	2.0 (0.7)	42.7 (1.0)	36.8 (0.9)	1.6 (1.1)	1.39 (0.11)	0.73 (0.14)
38	2.1 (0.6)	45.0 (3.7)	34.5 (2.5)	0.5 (1.1)	1.46 (0.34)	0.79 (0.19)
40	1.0 (0.9)	47.9 (3.4)	34.4 (2.3)	1.7 (2.1)	1.54 (0.38)	0.97 (0.29)
42	1.0 (0.9)	52.5 (4.9)	29.9 (3.2)	1.7 (2.1)	1.65 (0.49)	0.81 (0.18)
44	3.6 (2.4)	48.6 (7.3)	33.7 (4.5)	4.2 (5.4)	1.15 (0.60)	0.70 (0.27)
46	6.6 (1.7)	59.7 (6.4)	21.6 (9.9)	18.6 (7.0)	1.68 (0.69)	1.16 (0.32)
48	7.6 (1.8)	60.4 (5.9)	23.1 (9.1)	15.1 (7.2)	1.80 (0.62)	0.97 (0.38)
54	8.5 (1.7)	70.7 (6.3)	19.2 (6.8)	13.7 (8.0)	2.17 (0.58)	0.79 (0.35)

Δ_p, because these variations are comparable with the typical uncertainties. In fact, the fitted hopping amplitudes should be regarded as a parametrization of the low-energy DOS, rather than an accurate determination of the microscopic Hamiltonian. We will see that two properties of the dispersion which characterize the low-energy DOS, e.g., the VHS energy and the Fermi velocity, show comparatively smaller uncertainties, and a systematic trend with increasing Δ_p.

The scattering rate Γ is small with a small variance, and a tendency to increase with increasing Δ_p. This reflects a trend in the average spectra to be broader for larger gaps. At energies below Ω_s, Γ provides the only broadening mechanism. This parameter is therefore well constrained by the line shape around zero bias. At higher energies and for the large gaps, additional broadening is provided by Γ_s. Values of $\sim$15 meV seem somewhat too large for Γ_s, when compared with available values for Bi-2212 and Bi-2223,[21,69] but we note that their uncertainty is also large. We find that Δ_0 is larger than Δ_p, and that the difference increases with increasing Δ_p. As discussed in Sec. III C, this is connected with Δq being larger than $1/a$, so that the pairing induced by the spin resonance is overcompensated by the downward renormalization of the energy levels. The fitted Ω_s are anticorrelated with Δ_p, as discussed further below, and consistently with previous studies.[39,40] Lastly, the dimensionless parameter α exhibits no clear trend. However the product $(\alpha t_1)^2$, which controls the coupling strength [Eq. (14)], increases steadily with increasing Δ_p. We discuss the coupling strength further in Sec. V C.

V. DISCUSSION

A. Electron-hole asymmetry and Van Hove singularity

The STS spectra exhibit systematic asymmetries between positive and negative bias, suggestive of an intrinsic electron-hole asymmetry. The asymmetries concern the height of the coherence peaks, the strength of the dip, and the conductance background, as highlighted in Fig. 7. In the model, any asymmetry can be traced back to the band structure. For instance, one often finds that the negative-energy coherence peak is taller if the energy ξ_M of the VHS is negative [but there are exceptions; see Fig. 3(a)]. There is also a simple relationship between ξ_M and the width and asymmetry of the dip,[39] as is clearly seen in Fig. 3(a). A wider and/or stronger dip at negative bias means that $\xi_M < 0$. In this respect, the series of spectra in Fig. 7 present two trends, which seem to have conflicting implications. On the one hand, the coherence peaks become more symmetric with increasing Δ_p, suggesting that ξ_M is negative for small gaps and approaches zero for larger gaps. On the other hand, there is a tendency for the dip to become wider and more asymmetric with increasing Δ_p, indicating that the VHS moves to lower energies with increasing Δ_p.

The fits confirm the latter view, with larger negative values of ξ_M for larger gaps [Fig. 8(a)]. This evolution is consistent with the interpretation that spectra with larger gaps correspond to more underdoped regions with higher electron densities. Extrapolating our results, we expect a VHS at positive energy for gap values lower than 24 meV, i.e., on the strongly overdoped side. We are not aware of any systematic
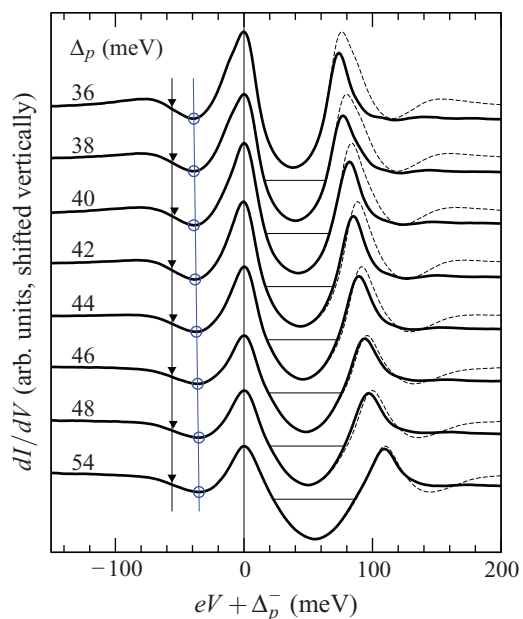
FIG. 7. (Color online) Average spectra of Fig. 2, with energies measured from one coherence peak. The dashed lines show the negative-bias spectrum, mirrored at positive energies to highlight the electron-hole asymmetry. The circles indicate the dip minimum, the triangles show the inflection point (peak in d^2I/dV^2), and the straight lines are guides to the eye.

investigation of the VHS by ARPES in Bi-2223. Reference 77 gives one point of comparison, with a dispersion approaching -25 meV at $(\pi,0)$, the value that we obtain for gaps close to 45 meV. However, this analysis neglects renormalization effects and may underestimate ξ_M.
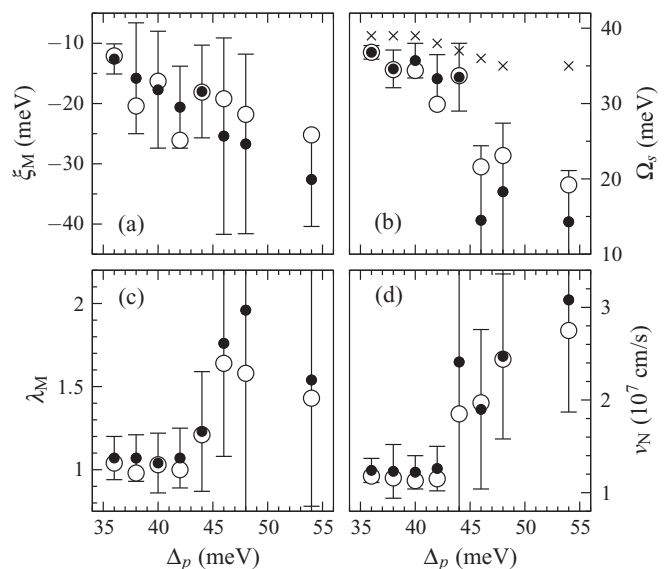
FIG. 8. Evolution of four properties with Δ_p. The empty symbols show the values obtained by fitting the average spectra. The full symbols with error bars show the average and standard deviation of the distributions obtained by fitting all individual spectra. The crosses in (b) represent the peak-to-dip energy difference of the average spectra, corresponding to the circles in Fig. 7. (c) Renormalization factor at the M point, Eq. (19). (d) Nodal velocity.

B. Spin-resonance energy

Figure 8(b) shows the fitted values of Ω_s. For the smallest gaps, corresponding to spectra with tall and asymmetric coherence peaks, we find values between 30 and 40 meV, and a good correspondence between Ω_s and the peak-to-dip energy difference. Both follow the same decreasing trend with increasing Δ_p. In classical superconductors, the phonon energies coincide with peaks in d^2I/dV^2.[8] We stress that in our spectra, the peak in d^2I/dV^2 occurs at an energy $\sim$56 meV (triangles in Fig. 7), similar to the values observed in Bi-2212.[78] This feature therefore does not provide a good estimate of Ω_s. This difference with classical superconductors is a consequence of the d-wave symmetry of the gap.[12,46] For gaps larger than 45 meV, Ω_s drops abruptly to values close to 20 meV, in contrast to the peak-to-dip energy, which stays close to 35 meV.

We believe that part of this drop is driven by changes in the spectra going beyond the scope of the model: The drop is accompanied by other changes, such as a raise of Γ_s and t_5 (see Table I), suggesting that the fit has moved to a different region of the parameter space. An obvious change between the 44 and 46 meV spectra is a falloff of the peak to background ratio. Increasing Γ and/or Γ_s cannot account for this, since it would also reduce the dip to background ratio, which remains unchanged in the spectra. The compromise is to lower Ω_s, and thus reduce the peak height without affecting the dip strength [see Fig. 3(b)], and to tune the position of the dip minimum by adjusting other parameters [in particular Δq; see Fig. 3(c)]. Another trend is that the coherence peaks become symmetric for large gaps, and this also drives Ω_s downward in the fits.

The range of Ω_s values in Fig. 8(b) corresponds well to the doping evolution observed by neutron scattering in Y-123, where the spin-resonance energy decreases from $\sim$40 meV at optimal doping to $\sim$25 meV in underdoped samples.[79,80] In Bi-2212, the resonance is found at 42 meV at optimal doping, and goes down to 34 meV with strong overdoping,[21] but no data have been reported in the underdoped region. Without neutron scattering data for Bi-2223, and considering the large variance of Ω_s for $\Delta_p > 45$ meV, it is difficult to ascertain whether the decrease of the spin-resonance energy for large gaps is as sudden as suggested by our fits, or rather more continuous.

C. Coupling strength and renormalization factors

The values of the bare coupling strength g obtained from our fits are similar to those used in Ref. 44. A more meaningful measure of the strength of self-energy effects is given by the renormalization factor

$$\lambda_k = -\frac{d}{d\omega}\frac{1}{2}\mathrm{Re}\big[\Sigma_{11}(\boldsymbol{k},\omega) + \Sigma_{22}(\boldsymbol{k},\omega)\big]_{\omega=0}. \quad (19)$$

Figure 8(c) shows the evolution of λ_k at the M point with varying Δ_p, and Fig. 9 shows the anisotropy of λ_k along the Fermi surface. λ_k is maximal at the antinodes and minimal at the nodes. The increase of λ_M above $\Delta_p = 45$ meV is accompanied by an increase of anisotropy: While the renormalization in antinodal and nodal regions differs by 20–30% for the smaller gaps, this increases to 30–50% for the larger gaps. Note that the λ_k shown in Fig. 9(a) are significantly larger, and more anisotropic, than the values found for Bi-2212
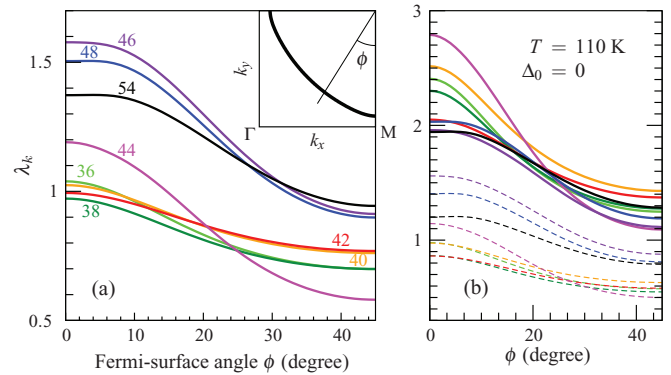
FIG. 9. (Color online) Renormalization factor λ_k along the renormalized Fermi surface. (a) Superconducting state: The parameters are those corresponding to the average spectra of Fig. 6 with the corresponding value of Δ_p written on each curve. Inset: Fermi surface for $\Delta_p = 42$ meV, and definition of the Fermi-surface angle ϕ. (b) Normal state: The solid lines show the value of λ_k obtained by setting $T = 110$ K and $\Delta_0 = 0$, and keeping the other parameters unchanged. The dashed lines correspond to $T = 110$ K, $\Delta_0 = 0$, and $\Gamma_s = 25$ meV.

using phonon models.[81] This suggests that a fit of phonon models to our STM data would yield unrealistically large electron-phonon matrix elements.

As the experimental determination of λ by ARPES and optical conductivity are mostly performed in the normal state, we have calculated λ_k at $T = T_c = 110$ K. Equation (15), which approximates the Brillouin-zone average of λ_k, shows that the renormalization *increases* in the normal state, because the gap in $N_0(\varepsilon)$ closes. Setting $T = 110$ K and $\Delta_0 = 0$, while keeping the other parameters unchanged, we obtain values of λ_k which are 1.2–2.4 times larger than in the superconducting state, and more anisotropic [Fig. 9(b)]. This calculation overlooks that the transition to the normal state also affects the spin resonance, which broadens in energy[82] on warming across T_c. This effect can be modeled by increasing Γ_s. As an illustration, we show in Fig. 9(b) the renormalization calculated with $\Gamma_s = 25$ meV (the normal-state value of Γ_s in Bi-2223 has not been determined experimentally). The values of λ_k are reduced and become similar to the values found in the superconducting state.

Our renormalization factors compare well with experimental values reported in the literature. In underdoped and overdoped Bi-2212, a normal-state renormalization of 1.5 near the antinodal point was determined by ARPES.[34] As the dip feature is stronger in Bi-2223 than in Bi-2212, a larger value may be expected for the three-layer compound. Indeed, the average renormalization in the normal state of Bi-2223 at optimal doping was estimated by fitting a model with a bosonic spectrum to optical data,[43] and leads to the values 2.18 and 1.75, depending on whether the full bosonic spectrum or its low-energy part is taken into account, respectively. In the normal state, but at the nodal point, a renormalization decreasing from 0.8 to 0.55 as a function of increasing hole doping was measured in Bi-2212 at 120 K.[83] Our nodal values for Bi-2223 in the normal state with $\Gamma_s = 25$ meV draw a similar trend, decreasing from 0.8 to 0.5 with decreasing gap size. Below T_c, nodal values between

0.7 and 0.9 are reported for Bi-2212 in Ref. 83. For optimally doped Bi-2223, a recent study[84] allows us to estimate a nodal renormalization of 0.6 at 10 K. These numbers are very close to our superconducting-state results of Fig. 9(a). Extracting the low-temperature antinodal renormalization from ARPES is difficult due to the gap. A study reported a value of 2 for optimally doped Bi-2212,[85] while our values for Bi-2223 vary between 1 and 1.6.

Figure 8(d) shows the nodal velocity, calculated using the fitted parameters and an in-plane lattice constant of 3.825 Å for Bi-2223. The nodal velocity can be measured directly by ARPES, unlike the renormalization (which requires an assumption for the bare dispersion). Reference 84 reports nodal velocities between 1.5 and 1.7 eV Å for the outer-layer band of optimally doped Bi-2223, corresponding to 2.3–2.6×10^7 cm/s. These values agree well with our results for $\Delta_p \gtrsim 44$ meV. In the case of Bi-2212, values ranging from 1 to 2.5×10^7 cm/s as a function of doping have been reported.[86] The variation seen in Fig. 8(d) can therefore be interpreted as reflecting changes in the local doping level.

D. Spectral function and simulated ARPES intensity

The parameters determined by fitting STM spectra allow us to calculate the momentum-resolved spectral function and to make predictions for the measured ARPES intensity. The generic properties of the spectral function in the model have been extensively discussed.[28,44] The main characteristics are summarized in Fig. 10. At energies below the onset of scattering, $|\omega| < \Omega_s$, the dispersion is renormalized downwards, but not broadened. This can be seen most clearly along the nodal direction $(0,0)$–(π,π) in Fig. 10(a). At these low energies, the quasiparticles form banana-shaped regions
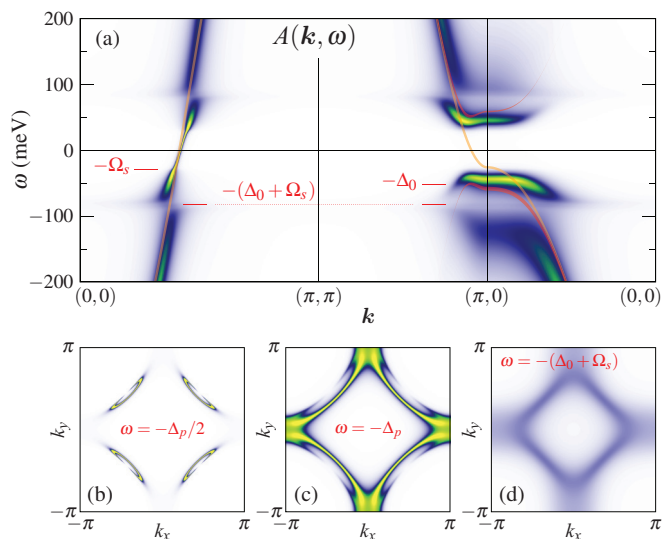
FIG. 10. (Color online) Spectral function calculated with the parameters fitted to the $\Delta_p = 42$ meV spectrum in Fig. 6. (a) Along high-symmetry lines in the Brillouin zone. The color scale shows the variation of the spectral function from zero (white) to its maximum (yellow). The orange line is the noninteracting dispersion. The red line shows the BCS dispersion; the width of the line is proportional to the spectral weight. (b), (c), and (d) Cuts at three characteristic energies. The color scale is the same in all graphs.

around the nodal points [Fig. 10(b)]. Increasing energy from the onset of scattering at Ω_s, the scattering rate increases and reaches its maximum at $\Delta_0 + \Omega_s$ [see Eq. (14)]. Since $\Delta_p \ll \Delta_0 + \Omega_s$, the antinodal excitations at $|\omega| = \Delta_p$ remain rather sharp [Fig. 10(c)]. When the scattering rate is maximum at $|\omega| = \Delta_0 + \Omega_s$, in contrast, the excitations are very broad [Fig. 10(d)]. At this energy, the real part of the self-energy changes sign, and the quasiparticle dispersion correspondingly jumps from below to above the noninteracting dispersion. This abrupt change in dispersion renormalization occurs *at the same energy in the whole Brillouin zone*, both for occupied and for empty states, and leads to a removal of spectral weight which is responsible for the dip in the DOS. Near the antinode, the d-wave gap induces additional structures: the minimum-gap locus is close to—but not exactly at—the position of the noninteracting Fermi surface along the $(\pi,0)$–(π,π) line, due to Fermi-surface renormalization. One also notices the reduction of the gap Δ_p with respect to Δ_0, due to the competition between pairing and renormalization (Sec. III C). In the low-energy region, the weakly dispersing quasiparticle branch near $(\pi,0)$ has lower energy than the corresponding BCS branch, while above the dip energy, the quasiparticle energy is higher than the noninteracting and BCS dispersions, like in the nodal region.

For a more quantitative comparison of our results with real ARPES data, we have simulated the upper panels of Fig. 2 in Ref. 87. We set the temperature to 10 K, and filter our spectral function with a Gaussian representing an energy resolution of 18 meV and a momentum resolution of $0.05/a$.[87] The result is displayed in Fig. 11. Close to the nodal direction (left and middle panels), the agreement is good. The model is too crude to completely capture the measured dispersion in the region of the dip: The simulated dispersion jumps from below to above the noninteracting dispersion, while the experiment interpolates smoothly across the jump. We attribute this discrepancy to additional scattering mechanisms not included in the model, in particular those involving the continuum of spin fluctuations.[44]

The energy of the "kink" around -70 meV is well reproduced by the calculation. We emphasize that the feature corresponding to the energy $\Delta_0 + \Omega_s$ is *not* the kink, but the midpoint of the jump, where the quasiparticle dispersion crosses the noninteracting dispersion. It is also worth stressing that this energy does not disperse, and is given by $\Delta_0 + \Omega_s$ at the node, in spite of the fact that the gap vanishes, as demonstrated in Fig. 10(a). The experimental determination of this energy scale by ARPES requires an assumption for the noninteracting dispersion. Our results call into question the assumption made in Ref. 87, that the quasiparticle and noninteracting dispersions meet near -200 meV. This assumption has direct implications for the value of the self-energy deduced from ARPES. In particular, the real part vanishes where the quasiparticle and noninteracting dispersions are equal, i.e., near -200 meV in Ref. 84. Using the dispersion from our fits, the real part of the self-energy would vanish at the energy $-(\Delta_0 + \Omega_s)$, which is consistent with a maximum of scattering rate at this energy. In the antinodal region (right panel of Fig. 11), there are differences between our results and the ARPES data: The low-energy part, below the kink, is too dispersive in the model, while the high-energy part is
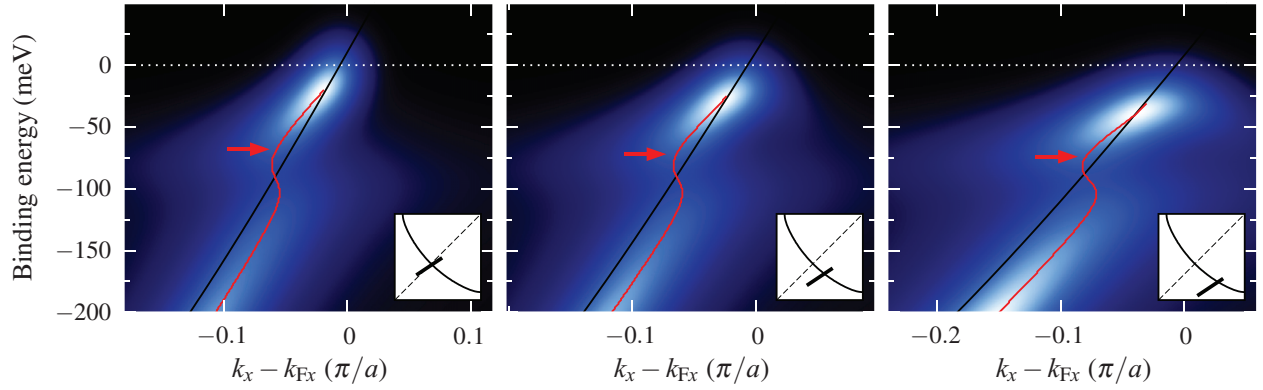
FIG. 11. (Color online) Simulated ARPES intensity for optimally doped Bi-2223 at $T = 10$ K. The spectral function of Fig. 10 was multiplied by the Fermi function, and filtered to mimic a momentum resolution of $0.05/a$ and an energy resolution of 18 meV. The color scale and the three momentum cuts correspond approximately to those of Fig. 2 in Ref. 87. The black lines show the noninteracting dispersion, and the red lines shows the quasiparticle dispersion (maximum of momentum distribution curves) for energies larger than the gap. The arrows indicate the "kink," where the quasiparticle dispersion deviates from its low-energy linear behavior.

not dispersive enough. This could be partly due to different Fermi surfaces in the experiment and in the model, which imply that the segments of the dispersion considered in both are not exactly identical. It could also be the consequence of scattering processes neglected in the model. Despite these differences, the kink energy and the minimum in the spectral intensity, between the low-energy and high-energy parts, are very similar. The overall agreement between Fig. 11 and Fig. 2 of Ref. 87 supports the claim that STM tunneling spectra, although they come from a momentum-integrating probe, do contain the necessary information needed to reconstruct the low-energy momentum-resolved spectral function.

VI. SUMMARY AND CONCLUSIONS

We have performed an analysis of STM spectra measured on optimally doped Bi-2223, by means of a strong-coupling model which takes into account the Van Hove singularity within a one-band description, a BCS gap with pure d-wave symmetry, and a coupling to the (π,π) spin resonance. This model can reproduce the experimental spectra (Fig. 6), with values of the parameters which are sound, and consistent with values obtained by other experimental probes. The inhomogeneity of the electronic properties on the sample surface allowed us to study variations in parameters as a function of the spectral gap Δ_p. Assuming a one-to-one correspondence between Δ_p and the hole doping level, changes in Δ_p may be interpreted as local variations of doping. The main trends are that the Van Hove singularity moves to lower energies with increasing Δ_p, and the energy of the spin resonance decreases (Fig. 8). The former supports the interpretation that larger gaps correspond to lower doping, and the latter supports the claim that the dip is caused by the spin resonance, rather than optical phonons. The strength of the coupling to the spin resonance, measured by the dispersion renormalization, increases steadily for gaps larger than 42 meV, namely towards the underdoped region of the phase diagram.

The presence of a Van Hove singularity, breaking the electron-hole symmetry of the electronic spectrum, is unmistakable in the raw data (Fig. 7). Nevertheless, the pre-

cise determination of the hopping amplitudes t_i remains a challenge, as illustrated by the large uncertainties attached to these parameters in Table I. The reason is that relatively large variations of the t_i's can collaborate to induce marginal changes in the electron DOS. Our confidence in the fitted tight-binding dispersion stems from the ability of the whole model to reproduce momentum-resolved ARPES data with good accuracy. In turn, our determination of the band structure may provide indications on how to extract the self-energy from ARPES measurements.

APPENDIX: THE FUNCTION $B(\omega,E)$

Equations (5) to (11) imply that the function $B(\omega,E)$ entering Eq. (13) reads

$$B(\omega,E) = \Lambda^2 \int_{-\infty}^{\infty} d\varepsilon_1 d\varepsilon_2 \left[L_{\Gamma_s}(\varepsilon_1 - \Omega_s) - L_{\Gamma_s}(\varepsilon_1 + \Omega_s) \right]$$
$$\times L_{\Gamma}(\varepsilon_2 - E) \frac{b(\varepsilon_1) + f(-\varepsilon_2)}{\omega - \varepsilon_1 - \varepsilon_2 + i0^+}, \quad \text{(A1)}$$

where b and f are the Bose and Fermi functions, respectively. Using the identity $\int dx\, L_{\Gamma}(x)/(z-x) = 1/[z + i\Gamma \operatorname{sign}(\operatorname{Im} z)]$, we obtain

$$\Lambda^{-2} B(\omega,E) = \int_{-\infty}^{\infty} d\varepsilon \frac{L_{\Gamma_s}(\varepsilon - \Omega_s) b(\varepsilon)}{\omega - E + i\Gamma - \varepsilon}$$
$$+ \int_{-\infty}^{\infty} d\varepsilon \frac{L_{\Gamma}(\varepsilon - E) f(-\varepsilon)}{\omega - \Omega_s + i\Gamma_s - \varepsilon}$$
$$- \{\Omega_s \rightarrow -\Omega_s\}. \quad \text{(A2)}$$

The symbol in braces means that the result obtained from the first two terms on the right-hand side must be antisymmetrized with respect to Ω_s. The remaining integrals can be evaluated by closing the integration contour in the complex plane. The

integrands can we rewritten in terms of products of simple poles by means of the identities

$$L_\Gamma(z) = \frac{1}{2\pi i}\left(\frac{1}{z - i\Gamma} - \frac{1}{z + i\Gamma}\right), \tag{A3}$$

$$b(z) = \frac{1}{\beta}\sum_{i\Omega_n}\frac{e^{i\Omega_n 0^+}}{z - i\Omega_n}, \tag{A4}$$

$$f(z) = -\frac{1}{\beta}\sum_{i\omega_n}\frac{e^{i\omega_n 0^+}}{z - i\omega_n}. \tag{A5}$$

Only one-half of the poles of the Bose or Fermi function are enclosed in the contour and give a contribution. Therefore, the integrals involve semi-infinite sums over Matsubara frequencies, which can be converted into the digamma function ψ, using the relation

$$\lim_{M\to\infty}\sum_{n=0}^{M}\frac{e^{\pm in0^+}}{n + z} = \ln M - \psi(z). \tag{A6}$$

The final result is

$$\Lambda^{-2}B(\omega,E) = \frac{b(\Omega_s - i\Gamma_s) + \frac{1}{2\pi i}\psi\left[\frac{\beta}{2\pi i}(\Omega_s - i\Gamma_s)\right]}{\omega - E - \Omega_s + i(\Gamma + \Gamma_s)} + \frac{\frac{\Gamma_s}{\pi}\psi\left[\frac{\beta}{2\pi i}(\omega - E + i\Gamma)\right]}{(\omega - E - \Omega_s + i\Gamma)^2 + \Gamma_s^2} - \frac{\frac{1}{2\pi i}\psi\left[\frac{\beta}{2\pi i}(\Omega_s + i\Gamma_s)\right]}{\omega - E - \Omega_s + i(\Gamma - \Gamma_s)}$$
$$+ \frac{f(-E + i\Gamma) + \frac{1}{2\pi i}\psi\left[\frac{1}{2} + \frac{\beta}{2\pi i}(E - i\Gamma)\right]}{\omega - E - \Omega_s + i(\Gamma + \Gamma_s)} + \frac{\frac{\Gamma}{\pi}\psi\left[\frac{1}{2} + \frac{\beta}{2\pi i}(\omega - \Omega_s + i\Gamma_s)\right]}{(\omega - E - \Omega_s + i\Gamma_s)^2 + \Gamma^2}$$
$$- \frac{\frac{1}{2\pi i}\psi\left[\frac{1}{2} + \frac{\beta}{2\pi i}(E + i\Gamma)\right]}{\omega - E - \Omega_s + i(\Gamma_s - \Gamma)} - \{\Omega_s \to -\Omega_s\}. \tag{A7}$$

The function B simplifies considerably in the case of a sharp resonance ($\Gamma_s = 0^+$) and for sharp Bogoliubov quasiparticles ($\Gamma = 0^+$), as well as zero temperature. In this case, we have

$$B(\omega,E) = \frac{\Lambda^2}{\omega - E - \Omega_s\,\text{sign}(E) + i0^+}, \tag{A8}$$

as can be readily deduced from Eq. (A1), by replacing the Lorentzians by delta functions.

---

*Present address: Low Temperatures Lab, Centro Atómico Bariloche, Argentina.

†Present address: Department of Physics and Astronomy, University of British Columbia, Vancouver, British Columbia V6T 1Z1, Canada.

[1] A. Damascelli, Z. Hussain, and Z.-X. Shen, Rev. Mod. Phys. **75**, 473 (2003).

[2] Ø. Fischer, M. Kugler, I. Maggio-Aprile, C. Berthod, and C. Renner, Rev. Mod. Phys. **79**, 353 (2007).

[3] C. Renner and Ø. Fischer, Phys. Rev. B **51**, 9208 (1995).

[4] P. Mallet, D. Roditchev, W. Sacks, D. Défourneau, and J. Klein, Phys. Rev. B **54**, 13324 (1996).

[5] A. Piriou, N. Jenkins, C. Berthod, I. Maggio-Aprile, and Ø. Fischer, Nat. Commun. **2**, 221 (2011).

[6] J. W. Alldredge, J. Lee, K. McElroy, M. Wang, K. Fujita, Y. Kohsaka, C. Taylor, H. Eisaki, S. Uchida, P. J. Hirschfeld, and J. C. Davis, Nat. Phys. **4**, 319 (2008).

[7] I. Giaever, H. R. Hart, Jr., and K. Megerle, Phys. Rev. **126**, 941 (1962).

[8] W. L. McMillan and J. M. Rowell, Phys. Rev. Lett. **14**, 108 (1965).

[9] Y. Fasano, I. Maggio-Aprile, N. D. Zhigadlo, S. Katrych, J. Karpinski, and O. Fischer, Phys. Rev. Lett. **105**, 167005 (2010).

[10] S. Chi, S. Grothe, R. Liang, P. Dosanjh, W. N. Hardy, S. A. Burke, D. A. Bonn, and Y. Pennec, Phys. Rev. Lett. **109**, 087002 (2012).

[11] J. F. Zasadzinski, L. Coffey, P. Romano, and Z. Yusof, Phys. Rev. B **68**, 180504(R) (2003).

[12] T. P. Devereaux, T. Cuk, Z.-X. Shen, and N. Nagaosa, Phys. Rev. Lett. **93**, 117004 (2004); S. Johnston and T. P. Devereaux, Phys. Rev. B **81**, 214512 (2010); S. Johnston, W. S. Lee, Y. Chen, E. A. Nowadnick, B. Moritz, Z.-X. Shen, and T. P. Devereaux, Adv. Condens. Matter Phys. **2010**, 968304 (2010).

[13] J. Nieminen, I. Suominen, T. Das, R. S. Markiewicz, and A. Bansil, Phys. Rev. B **85**, 214504 (2012).

[14] T. Cren, D. Roditchev, W. Sacks, and J. Klein, Europhys. Lett. **52**, 203 (2000); W. Sacks, T. Cren, D. Roditchev, and B. Douçot, Phys. Rev. B **74**, 174517 (2006).

[15] A. C. Fang, L. Capriotti, D. J. Scalapino, S. A. Kivelson, N. Kaneko, M. Greven, and A. Kapitulnik, Phys. Rev. Lett. **96**, 017007 (2006).

[16] A. M. Gabovich and A. I. Voitenko, Phys. Rev. B **75**, 064516 (2007).

[17] J. Rossat-Mignod, L. P. Regnault, C. Vettier, P. Bourges, P. Burlet, J. Bossy, J. Y. Henry, and G. Lapertot, Physica C **185**, 86 (1991).

[18] H. A. Mook, M. Yethiraj, G. Aeppli, T. E. Mason, and T. Armstrong, Phys. Rev. Lett. **70**, 3490 (1993).

[19] G. Yu, Y. Li, E. M. Motoyama, X. Zhao, N. Barišić, Y. Cho, P. Bourges, K. Hradil, R. A. Mole, and M. Greven, Phys. Rev. B **81**, 064518 (2010).

[20] H. He, P. Bourges, Y. Sidis, C. Ulrich, L. P. Regnault, S. Pailhès, N. S. Berzigiarova, N. N. Kolesnikov, and B. Keimer, Science **295**, 1045 (2002); B. Keimer, H. He, P. Bourges, Y. Sidis, C. Ulrich, L. P. Regnault, S. Pailhès, N. S. Berzigiarova, and N. N. Kolesnikov, J. Phys. Chem. Solids **63**, 2243 (2002).

[21] H. F. Fong, P. Bourges, Y. Sidis, L. P. Regnault, A. Ivanov, G. D. Gu, N. Koshizuka, and B. Keimer, Nature (London) **398**, 588 (1999); L. Capogna, B. Fauqué, Y. Sidis, C. Ulrich, P. Bourges, S. Pailhès, A. Ivanov, J. L. Tallon, B. Liang, C. T. Lin, A. I. Rykov,

and B. Keimer, Phys. Rev. B **75**, 060502 (2007); B. Fauqué, Y. Sidis, L. Capogna, A. Ivanov, K. Hradil, C. Ulrich, A. I. Rykov, B. Keimer, and P. Bourges, *ibid.* **76**, 214512 (2007).

[22] J. Mesot, N. Metoki, M. Böhm, A. Hiess, and K. Kadowaki, Physica C **341**, 2105 (2000).

[23] G. Xu, G. D. Gu, M. Hücker, B. Fauqué, T. G. Perring, L. P. Regnault, and J. M. Tranquada, Nat. Phys. **5**, 642 (2009).

[24] S. D. Wilson, P. Dai, S. Li, S. Chi, H. J. Kang, and J. W. Lynn, Nature (London) **442**, 49 (2006).

[25] Y. Sidis, S. Pailhès, B. Keimer, P. Bourges, C. Ulrich, and L. P. Regnault, Phys. Status Solidi B **241**, 1204 (2004).

[26] H. He, Y. Sidis, P. Bourges, G. D. Gu, A. Ivanov, N. Koshizuka, B. Liang, C. T. Lin, L. P. Regnault, E. Schoenherr, and B. Keimer, Phys. Rev. Lett. **86**, 1610 (2001).

[27] C. Stock, W. J. L. Buyers, R. Liang, D. Peets, Z. Tun, D. Bonn, W. N. Hardy, and R. J. Birgeneau, Phys. Rev. B **69**, 014502 (2004).

[28] See, e.g., M. Eschrig, Adv. Phys. **55**, 47 (2006), and references therein.

[29] P. W. Anderson, Science **317**, 1705 (2007).

[30] T. A. Maier, D. Poilblanc, and D. J. Scalapino, Phys. Rev. Lett. **100**, 237001 (2008).

[31] H.-Y. Kee, S. A. Kivelson, and G. Aeppli, Phys. Rev. Lett. **88**, 257002 (2002).

[32] A. Abanov, A. V. Chubukov, M. Eschrig, M. R. Norman, and J. Schmalian, Phys. Rev. Lett. **89**, 177002 (2002).

[33] M. R. Norman, H. Ding, J. C. Campuzano, T. Takeuchi, M. Randeria, T. Yokoya, T. Takahashi, T. Mochiku, and K. Kadowaki, Phys. Rev. Lett. **79**, 3506 (1997); J. C. Campuzano, H. Ding, M. R. Norman, H. M. Fretwell, M. Randeria, A. Kaminski, J. Mesot, T. Takeuchi, T. Sato, T. Yokoya, T. Takahashi, T. Mochiku, K. Kadowaki, P. Guptasarma, D. G. Hinks, Z. Konstantinovic, Z. Z. Li, and H. Raffy, *ibid.* **83**, 3709 (1999); A. Kaminski, M. Randeria, J. C. Campuzano, M. R. Norman, H. Fretwell, J. Mesot, T. Sato, T. Takahashi, and K. Kadowaki, *ibid.* **86**, 1070 (2001).

[34] T. K. Kim, A. A. Kordyuk, S. V. Borisenko, A. Koitzsch, M. Knupfer, H. Berger, and J. Fink, Phys. Rev. Lett. **91**, 167002 (2003); S. V. Borisenko, A. A. Kordyuk, T. K. Kim, A. Koitzsch, M. Knupfer, M. S. Golden, J. Fink, M. Eschrig, H. Berger, and R. Follath, *ibid.* **90**, 207001 (2003); V. B. Zabolotnyy, S. V. Borisenko, A. A. Kordyuk, J. Fink, J. Geck, A. Koitzsch, M. Knupfer, B. Büchner, H. Berger, A. Erb, C. T. Lin, B. Keimer, and R. Follath, *ibid.* **96**, 037003 (2006); S. V. Borisenko, A. A. Kordyuk, A. Koitzsch, J. Fink, J. Geck, V. Zabolotnyy, M. Knupfer, B. Büchner, H. Berger, M. Falub, M. Shi, J. Krempasky, and L. Patthey, *ibid.* **96**, 067001 (2006).

[35] A. D. Gromko, A. V. Fedorov, Y.-D. Chuang, J. D. Koralek, Y. Aiura, Y. Yamaguchi, K. Oka, Y. Ando, and D. S. Dessau, Phys. Rev. B **68**, 174520 (2003).

[36] T. Sato, H. Matsui, T. Takahashi, H. Ding, H.-B. Yang, S.-C. Wang, T. Fujii, T. Watanabe, A. Matsuda, T. Terashima, and K. Kadowaki, Phys. Rev. Lett. **91**, 157003 (2003).

[37] J. F. Zasadzinski, L. Ozyuzer, N. Miyakawa, K. E. Gray, D. G. Hinks, and C. Kendziora, Phys. Rev. Lett. **87**, 067005 (2001).

[38] B. W. Hoogenboom, C. Berthod, M. Peter, Ø. Fischer, and A. A. Kordyuk, Phys. Rev. B **67**, 224502 (2003).

[39] G. Levy de Castro, C. Berthod, A. Piriou, E. Giannini, and Ø. Fischer, Phys. Rev. Lett. **101**, 267004 (2008).

[40] N. Jenkins, Y. Fasano, C. Berthod, I. Maggio-Aprile, A. Piriou, E. Giannini, B. W. Hoogenboom, C. Hess, T. Cren, and Ø. Fischer, Phys. Rev. Lett. **103**, 227001 (2009).

[41] F. C. Niestemski, S. Kunwar, S. Zhou, S. Li, H. Ding, Z. Wang, P. Dai, and V. Madhavan, Nature (London) **450**, 1058 (2007).

[42] J. P. Carbotte, E. Schachinger, and D. N. Basov, Nature (London) **401**, 354 (1999); J. J. Tu, C. C. Homes, G. D. Gu, D. N. Basov, and M. Strongin, Phys. Rev. B **66**, 144514 (2002); J. Hwang, T. Timusk, and G. D. Gu, Nature (London) **427**, 714 (2004); J. Yang, J. Hwang, E. Schachinger, J. P. Carbotte, R. P. S. M. Lobo, D. Colson, A. Forget, and T. Timusk, Phys. Rev. Lett. **102**, 027003 (2009).

[43] E. van Heumen, E. Muhlethaler, A. B. Kuzmenko, H. Eisaki, W. Meevasana, M. Greven, and D. van der Marel, Phys. Rev. B **79**, 184512 (2009); E. van Heumen, W. Meevasana, A. B. Kuzmenko, H. Eisaki, and D. van der Marel, New J. Phys. **11**, 055067 (2009).

[44] M. Eschrig and M. R. Norman, Phys. Rev. Lett. **85**, 3261 (2000); Phys. Rev. B **67**, 144503 (2003).

[45] J. R. Schrieffer, D. J. Scalapino, and J. W. Wilkins, Phys. Rev. Lett. **10**, 336 (1963).

[46] C. Berthod, Phys. Rev. B **82**, 024504 (2010).

[47] M. Kugler, G. Levy de Castro, E. Giannini, A. Piriou, A. A. Manuel, C. Hess, and Ø. Fischer, J. Phys. Chem. Solids **67**, 353 (2006).

[48] T. Sato, H. Matsui, S. Nishina, T. Takahashi, T. Fujii, T. Watanabe, and A. Matsuda, Phys. Rev. Lett. **89**, 067005 (2002).

[49] D. L. Feng, A. Damascelli, K. M. Shen, N. Motoyama, D. H. Lu, H. Eisaki, K. Shimizu, J.-i. Shimoyama, K. Kishio, N. Kaneko, M. Greven, G. D. Gu, X. J. Zhou, C. Kim, F. Ronning, N. P. Armitage, and Z.-X. Shen, Phys. Rev. Lett. **88**, 107001 (2002).

[50] H. Matsui, T. Sato, T. Takahashi, H. Ding, H.-B. Yang, S.-C. Wang, T. Fujii, T. Watanabe, A. Matsuda, T. Terashima, and K. Kadowaki, Phys. Rev. B **67**, 060501(R) (2003).

[51] P. W. Anderson and N. P. Ong, J. Phys. Chem. Solids **67**, 1 (2006); P. W. Anderson, Int. J. Mod. Phys. B **25**, 1 (2011).

[52] E. Giannini, V. Garnier, R. Gladyshevskii, and R. Flükiger, Supercond. Sci. Technol. **17**, 220 (2004).

[53] A. Piriou, Y. Fasano, E. Giannini, and Ø. Fischer, Phys. Rev. B **77**, 184508 (2008).

[54] E. Giannini, N. Clayton, N. Musolino, A. Piriou, R. Gladyshevskii, and R. Flükiger, IEEE Trans. Appl. Supercond. **15**, 3102 (2005).

[55] E. Giannini, R. Gladyshevskii, N. Clayton, N. Musolino, V. Garnier, A. Piriou, and R. Flükiger, Curr. App. Phys. **8**, 115 (2008).

[56] A. Piriou, Y. Fasano, E. Giannini, and Ø. Fischer, Physica C **460-462**, 408 (2007).

[57] M. Kugler, C. Renner, V. Mikheev, G. Batey, and Ø. Fischer, Rev. Sci. Instrum. **71**, 1475 (2000).

[58] J. Tersoff and D. R. Hamann, Phys. Rev. Lett. **50**, 1998 (1983).

[59] R. C. Dynes, V. Narayanamurti, and J. P. Garno, Phys. Rev. Lett. **41**, 1509 (1978).

[60] M. Mori, T. Tohyama, and S. Maekawa, Phys. Rev. B **66**, 064502 (2002).

[61] S. Ideta, K. Takashima, M. Hashimoto, T. Yoshida, A. Fujimori, H. Anzai, T. Fujita, Y. Nakashima, A. Ino, M. Arita, H. Namatame, M. Taniguchi, K. Ono, M. Kubota, D. H. Lu, Z.-X. Shen, K. M. Kojima, and S. Uchida, Phys. Rev. Lett. **104**, 227001 (2010); Physica C **470**, S14 (2010).

[62] P. Xu, Ph.D. thesis, École Polytechnique Fédérale de Lausanne, 2010.

[63] L. Tewordt, J. Low Temp. Phys. **15**, 349 (1973).

[64] D. J. Scalapino, E. Loh, and J. E. Hirsch, Phys. Rev. B **34**, 8190 (1986).

[65] S. Lenck, S. Wermbter, and L. Tewordt, J. Low Temp. Phys. **80**, 269 (1990).

[66] P. Monthoux, A. V. Balatsky, and D. Pines, Phys. Rev. Lett. **67**, 3448 (1991).

[67] P. Monthoux, Phys. Rev. B **70**, 144403 (2004).

[68] S. Wermbter and L. Tewordt, Physica C **211**, 132 (1993).

[69] S. Pailès, Ph.D. thesis, Université Paris 6, 2004.

[70] P. Bourges, Y. Sidis, H. F. Fong, L. P. Regnault, J. Bossy, A. Ivanov, and B. Keimer, Science **288**, 1234 (2000); D. Reznik, P. Bourges, L. Pintschovius, Y. Endoh, Y. Sidis, T. Masui, and S. Tajima, Phys. Rev. Lett. **93**, 207003 (2004).

[71] G. D. Mahan, *Many Particle Physics*, 3rd ed. (Plenum, New York, 2000).

[72] It is possible to find different sets of tight-binding parameters which give hardly distinguishable noninteracting DOS in a limited energy window. For instance, the widely different sets $(\mu, t_1, t_2, t_3, t_4, t_5) = (-192, -250, 52, -16, 2, 13)$ meV and $(-12, -158, 4, -6, 6, 0)$ meV yield identical DOS, up to a multiplicative constant, in the energy range $|\omega| < 150$ meV.

[73] The usual least-squares function, $F = \sum_i (y_i - Y_i)^2$, measures the vertical distance between two curves $y_i(x_i)$ and $Y_i(X_i)$. This is not optimal for curves with nearly vertical segments, such as steep coherence peaks, because a tiny horizontal mismatch is strongly penalized. We use a different measure of the distance between two curves: For each point of the first curve, we calculate the shortest Cartesian distance to any point of the second curve: $\tilde{F} = \sum_i \min_k [(x_i - X_k)^2 + (y_i - Y_k)^2]$. We minimize this function with the Levenberg-Marquardt algorithm.

[74] M. R. Norman, M. Randeria, H. Ding, and J. C. Campuzano, Phys. Rev. B **52**, 615 (1995).

[75] A. A. Kordyuk, S. V. Borisenko, M. Knupfer, and J. Fink, Phys. Rev. B **67**, 064504 (2003).

[76] M. Hashimoto, T. Yoshida, H. Yagi, M. Takizawa, A. Fujimori, M. Kubota, K. Ono, K. Tanaka, D. H. Lu, Z.-X. Shen, S. Ono, and Y. Ando, Phys. Rev. B **77**, 094516 (2008).

[77] H. Matsui, T. Sato, T. Takahashi, S.-C. Wang, H.-B. Yang, H. Ding, T. Fujii, T. Watanabe, and A. Matsuda, Phys. Rev. Lett. **90**, 217002 (2003).

[78] J. Lee, K. Fujita, K. McElroy, J. A. Slezak, M. Wang, Y. Aiura, H. Bando, M. Ishikado, T. Masui, J. X. Zhu, A. V. Balatsky, H. Eisaki, S. Uchida, and J. C. Davis, Nature (London) **442**, 546 (2006).

[79] P. Bourges, L. P. Regnault, J. Y. Henry, C. Vettier, Y. Sidis, and P. Burlet, Physica B **215**, 30 (1995).

[80] H. F. Fong, B. Keimer, D. L. Milius, and I. A. Aksay, Phys. Rev. Lett. **78**, 713 (1997).

[81] S. Johnston, F. Vernay, B. Moritz, Z.-X. Shen, N. Nagaosa, J. Zaanen, and T. P. Devereaux, Phys. Rev. B **82**, 064513 (2010).

[82] L. P. Regnault, P. Bourges, P. Burlet, J. Y. Henry, J. Rossat-Mignod, Y. Sidis, and C. Vettier, Physica B **213**, 48 (1995).

[83] A. A. Kordyuk, S. V. Borisenko, V. B. Zabolotnyy, J. Geck, M. Knupfer, J. Fink, B. Büchner, C. T. Lin, B. Keimer, H. Berger, A. V. Pan, S. Komiya, and Y. Ando, Phys. Rev. Lett. **97**, 017002 (2006).

[84] S. Ideta, T. Yoshida, M. Hashimoto, A. Fujimori, H. Anzai, A. Ino, M. Arita, H. Namatame, M. Taniguchi, K. Takashima, K. M. Kojima, and S. Uchida, J. Phys.: Conf. Ser. **428**, 012039 (2013).

[85] J. Fink, A. Koitzsch, J. Geck, V. Zabolotnyy, M. Knupfer, B. Buchner, A. Chubukov, and H. Berger, Phys. Rev. B **74**, 165102 (2006).

[86] I. M. Vishik, W. S. Lee, R.-H. He, M. Hashimoto, Z. Hussain, T. P. Devereaux, and Z.-X. Shen, New J. Phys. **12**, 105008 (2010).

[87] S. Ideta, K. Takashima, M. Hashimoto, T. Yoshida, A. Fujimori, M. Kubota, K. Ono, K. Kojima, and S. Uchida, J. Phys.: Conf. Ser. **108**, 012015 (2008).